Materials Research Letters

ISSN: (Print) (Online) Journal homepage: https://www.tandfonline.com/loi/tmrl20

The role of *in-situ* nano-TiB_2 particles in improving the printability of noncastable 2024Al alloy

Tengteng Sun, Hongze Wang, Zhenyang Gao, Yi Wu, Mingliang Wang, Xinyuan Jin, Chu Lun Alex Leung, P.D. Lee, Yanan Fu & Haowei Wang

To cite this article: Tengteng Sun, Hongze Wang, Zhenyang Gao, Yi Wu, Mingliang Wang, Xinyuan Jin, Chu Lun Alex Leung, P.D. Lee, Yanan Fu & Haowei Wang (2022) The role of *in-situ* nano-TiB_2 particles in improving the printability of noncastable 2024Al alloy, Materials Research Letters, 10:10, 656-665, DOI: 10.1080/21663831.2022.2080514

To link to this article: https://doi.org/10.1080/21663831.2022.2080514

MATER. RES. LETT.
2022, VOL. 10, NO. 10, 656–665
https://doi.org/10.1080/21663831.2022.2080514

MATERIALS RESEARCH LETTERS
Taylor & Francis
Taylor & Francis Group

ORIGINAL REPORTS

The role of *in-situ* nano-TiB_2 particles in improving the printability of noncastable 2024Al alloy

Tengteng Sun[a,b], Hongze Wang[a,b,d,e], Zhenyang Gao[a,b], Yi Wu[a,b,c], Mingliang Wang[a,b], Xinyuan Jin[a,b], Chu Lun Alex Leung[d,e], P.D. Lee[d,e], Yanan Fu[f] and Haowei Wang[a,b]

[a]State Key Laboratory of Metal Matrix Composites, Shanghai Jiao Tong University, Shanghai, People's Republic of China; [b]School of Materials Science & Engineering, Shanghai Jiao Tong University, Shanghai, People's Republic of China; [c]Institute of Alumics Materials, Shanghai Jiao Tong University (Anhui), Huaibei, People's Republic of China; [d]Department of Mechanical Engineering, University College London, London, UK; [e]Research Complex at Harwell, Harwell Campus, Oxfordshire, UK; [f]Shanghai Synchrotron Radiation Facility/Zhangjiang Lab, Shanghai Advanced Research Institute, Chinese Academy of Sciences, Shanghai, People's Republic of China

ABSTRACT

In-situ pre-decorated different content of TiB_2 particle reinforced 2024 Al matrix composites (xTiB$_2$/2024Al composite, x = 0, 1, 2, 4, 6, 8 wt.%) were printed by laser powder bed fusion (LPBF). A quantitative equation was established to quantify heterogeneous nucleating potency by TiB_2 nanoparticles on the grain size of the LPBFed samples. Optimized mechanical properties were obtained in the as-printed 4TiB$_2$/2024Al alloy which proved the feasibility of replacing the wrought part with the LPBFed one. This manuscript provides a method to determine the optimized content of TiB_2 nanoparticles to change the noncastable material to the printable one.

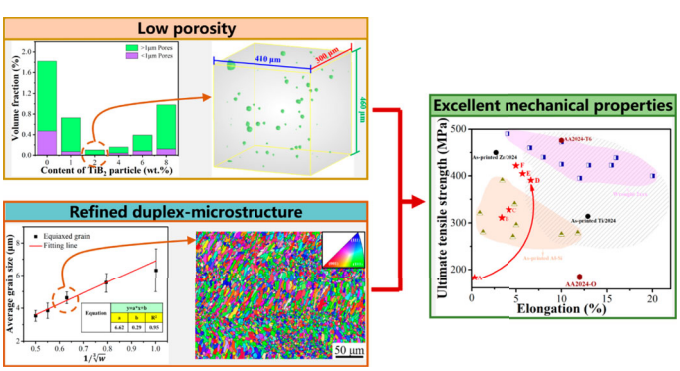

ARTICLE HISTORY
Received 14 March 2022

KEYWORDS
Laser powder bed fusion; composites; grain refinement efficiency; heterogeneous nucleating

IMPACT STATEMENT

This manuscript provides a method to determine the optimized TiB_2 content to change the non-castable material to the printable one, and can potentially guide the introduction of many other nanoparticles.

1. Introduction

Laser powder bed fusion (LPBF) is a revolutionary additive manufacturing (AM) technique with short productive cycle and high material utilization [1, 2]. A high cooling rate of 10^3–10^7 K/s can be achieved during the LPBF process, providing a chance for printing high-strength materials with unique fine and metastable microstructures [3]. It has received increasing attention from many industry fields, including aerospace, mold, and so on [4, 5].

Wrought 2024Al alloy (Al-4.2Cu-1.6Mg-0.6Mn) has the advantages of higher strength and lower density,

CONTACT Hongze Wang hz.wang@sjtu.edu.cn State Key Laboratory of Metal Matrix Composites, Shanghai Jiao Tong University, Shanghai, People's Republic of China; School of Materials Science & Engineering, Shanghai Jiao Tong University, Shanghai, People's Republic of China; Department of Mechanical Engineering, University College London, London, WC1E 7JE, UK; Research Complex at Harwell, Harwell Campus, Oxfordshire, OX11 0FA, UK; Yi Wu eagle51@sjtu.edu.cn State Key Laboratory of Metal Matrix Composites, Shanghai Jiao Tong University, Shanghai, People's Republic of China; Mingliang Wang, mingliang_wang@sjtu.edu.cn State Key Laboratory of Metal Matrix Composites, Shanghai Jiao Tong University, People's Republic of China; School of Materials Science & Engineering, Shanghai Jiao Tong University, People's Republic of China

Supplemental data for this article can be accessed here. https://doi.org/10.1080/21663831.2022.2080514

meaning that it has promising prospects in aerospace [6, 7]. In recent years, there is an increasing demand for components with complicated geometrical designs, which is beyond the capability of conventional manufacturing methods. However, when considering LPBF, 2024Al alloy usually exhibits poor printability due to its high cracking susceptibility [8]. Some research is devoted to improving the printability of wrought Al alloys by introducing inoculates. Many effective inoculates have been proposed to be applied such as TiC [9], TiB_2 [10], TiB + TiC [11], ZrH_2 [12], SiO_2 [13], Er [14], etc. They proposed that introducing nanoparticles as the nucleating agent to crack-susceptible alloys can induce large amounts of equiaxed grain with a high capacity of accommodating strain, thereby inhibiting hot cracking effectively during solidification. Nevertheless, there are limited research related to the efficiency of these inoculates. The key challenge of this paper is to quantify the relationship between nanoparticle content and defect content, grain refinement level, as well as mechanical properties of the printed material.

Currently, research to introduce inoculators to modify the alloy powder for LPBF is mainly concentrated on the mechanical mixing method [14]. Although it is effective but hard to apply for mass production. While the *in-situ* method is easier to apply. TiB_2 is an ideal heterogeneous nucleation agent to study the grain refinement efficiency and strengthening mechanisms of ceramic particles [15, 16]. This paper uses the basis rooted in interdependence theory, a quantitative relationship between TiB_2 particle content and grain size is proposed, which can be utilized to predict and control the grain size of TiB_2 particle reinforced composites under the LPBF process.

2. Materials

The compositions of powder were measured by inductively coupled-atomic emission spectrometry (ICP-AES, iCAP7600, Table 1). Moreover, as-printed 2024Al and $x$$TiB_2$/2024Al ($x$ = 1, 2, 4, 6, 8 wt.%) composites were fabricated in Prox DMP 200 LPBF machine (3D Systems, USA). Detailed experimental procedures were shown in *Supplementary material*.

3. Results and discussion

Figure 1(a-f) shows a three-dimensional visualization of pores in the as-printed samples obtained by the X-ray CT. The pores were rendered in two colors according to their sizes with a boundary of 1 μm. Typically, as-printed 2024Al alloy had a significantly larger number and total volume fraction of pores ($1.86 \pm 0.64\%$, Figure 1(a and g)). With the TiB_2 addition (Figure 1(b-g)), a good printability of composites can be confirmed by the absence of large-size defects (i.e. solidification cracks or other obvious incomplete fusion holes). In detail, the volume fraction of pores decreased first and then increased with the TiB_2 content increase. Critically, the as-printed 2TiB_2/2024Al composite showed a turning point with the pore volume fraction of $0.09 \pm 0.03\%$ (Figure 1(c and g)). In particular, the number of smaller pores (≤ 1 μm) was decreased significantly with TiB_2 nanoparticles addition. Although the larger pores (> 1 μm) cannot be eliminated, they showed a substantial reduction (Figure 1(g)). Figure 1(h) shows the relationship between macroscopic relative density and TiB_2 content determined by Archimedes'principle-based measurements [17]. The result was consistent with the tendency of X-ray CT, in which the maximum relative density was obtained in as-printed 2TiB_2/2024Al composite. In Figure 1(i), the reflectivity of $x$$TiB_2$/2024Al composite powders is significantly lower than that of 2024Al alloy powder ($53.98 \pm 0.56\%$). For instance, laser absorption of 8TiB_2/2024Al powder is more than 2 times higher than the pure alloy at the laser wavelength of LPBF machine, *i.e.* 1070 nm.

The pre-decorated TiB_2 nanoparticles are found to exhibit two mutually exclusive effects on printability in LPBF. (1) The laser reflectivity decreases with the increasing TiB_2 content. After laser irradiation on the powder bed, the laser beam will be reflected and absorbed several times between the composite powder surfaces [18]. When introducing TiB_2 nanoparticles, they can cover the powder surface to absorb part of energy, and then be transferred to the surrounding powder by heat conduction. This is also known as the radiation conduction described in ref. [19]. Therefore, laser energy acting directly on the substrate powder will be reduced. (2) An increasing TiB_2 content has led to an increase in the viscosity of Al alloy melt [20]. With an increased viscosity, the fluidity of the molten material decreases, which may mitigate the escape of gases from the molten pool. Probably, the formation of open pores is partially attributed to this aspect. The effects of viscosity and formation of open pores have been previously observed in LPBF of 13–93 bioactive glass and fuzed silica [19, 21] because the viscosity of glass is *ca.* 1000 times greater than that of metallic melt pool.

According to the Einstein-Roscoe model of fluid viscosity of composites [22]:

$$\mu = \mu_0(1 - f)^{-2.5} \tag{1}$$

where μ is the viscosity of the composite melt, μ_0 is the viscosity of pure alloy, f is the TiB_2 content. In the Al melt, greater melt viscosity induces a lower fluidity with higher

Table 1. Chemical compositions and theoretical density (ρ) of the experimental material calculated by JMatPro.

Powder type	Al (wt.%)	Cu (wt.%)	Mg (wt.%)	Mn (wt.%)	Ti (wt.%)	B (wt.%)	ρ (g/cm^3)
2024Al	Bal.	4.21	1.58	0.60	–	–	2.77
1TiB$_2$/2024Al	Bal.	4.4	1.6	0.6	0.58	0.27	2.78
2TiB$_2$/2024Al	Bal.	4.11	1.58	0.61	1.38	0.61	2.79
4TiB$_2$/2024Al	Bal.	4.01	1.51	0.59	2.86	1.21	2.81
6TiB$_2$/2024Al	Bal.	4.12	1.53	0.58	4.38	1.99	2.84
8TiB$_2$/2024Al	Bal.	4.12	1.46	0.55	5.57	2.60	2.87

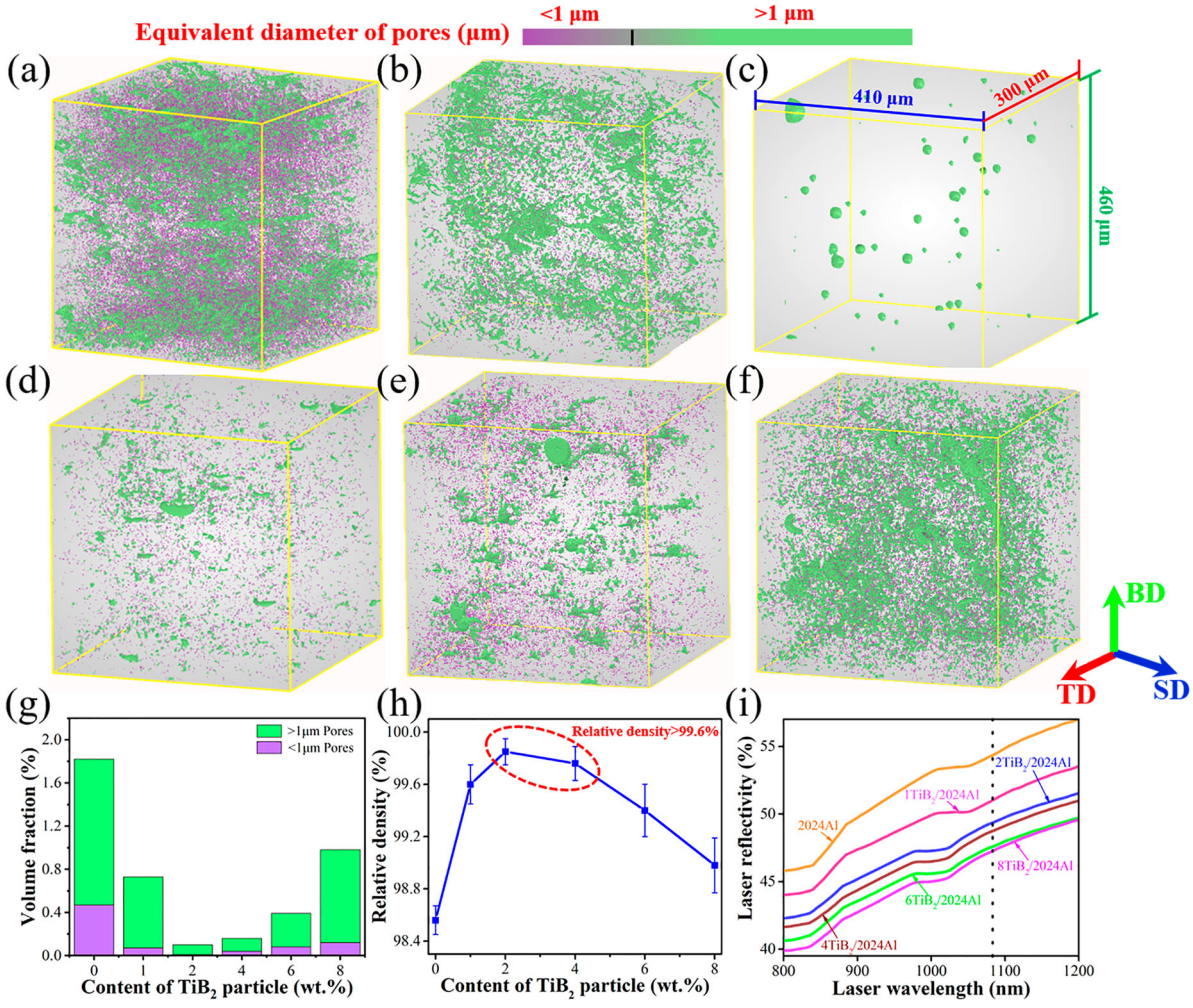

Figure 1. X-ray CT results of porosity in as-printed (a) 2024Al alloy, (b-f) xTiB$_2$/2024Al composites (x = 1, 2, 4, 6, 8 wt.%), (g) volume fraction of pores with average size divided by 1 μm, (h) relative density of as-printed samples and (i) reflectivity of the powders. The dashed vertical line indicates the laser wavelength at 1070 nm.

TiB$_2$ content. This weakens the wetting characteristics of the melt and further reduces metallurgical bonding between layers and affects the printability [23].

To understand the effect of TiB$_2$ content on the grain structure and texture information of as-printed specimens, we used SEM-EBSD to examine these materials. EBSD orientation maps of the α-Al phase in the SD-BD plane are provided in Figure 2(a-f) for as-printed samples. Figure 2(a) shows an inhomogeneity grain morphology showing a coarse columnar grain predominantly orientating parallel to the build direction in 2024Al alloy. Unlike the columnar grain structure in 2024Al alloy, in Figure 2(b-f), a classic duplex-microstructure consisting of fine equiaxed at the top of melt pools and coarse columnar grains at the bottom of melt pool was obtained in the as-printed xTiB$_2$/2024Al composite. The duplex-microstructure formed is attributed to the rapid cooling rate during the LPBF process, heterogeneous nucleation, and the pinning grain boundary effects provided by TiB$_2$ nanoparticles [24]. With an increase in TiB$_2$ content, a reduced number and size of the columnar grains are observed in composites, see analysis later. Figure 2(g-l)

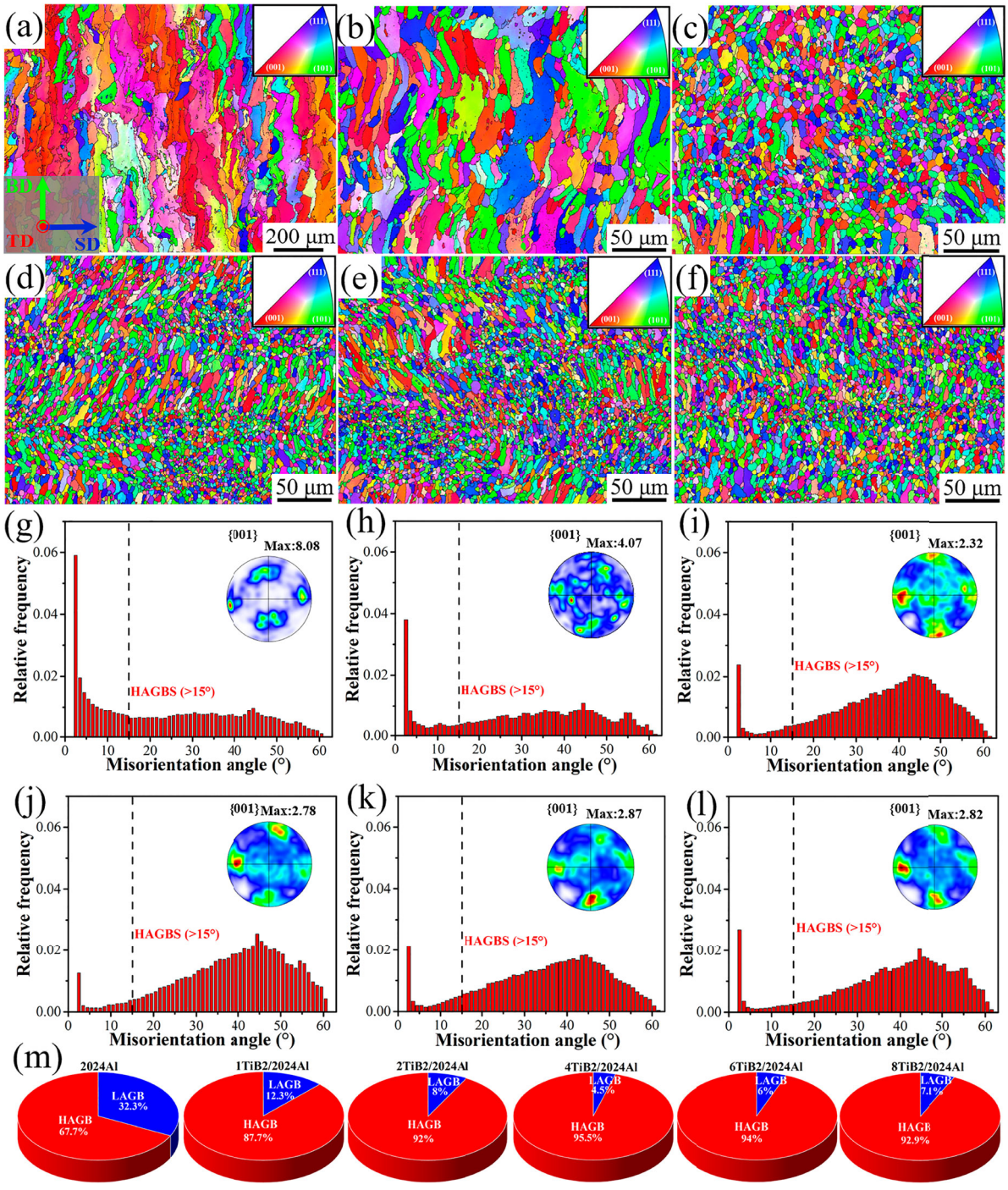

Figure 2. EBSD maps for as-printed (a) 2024Al, (b-f) xTiB$_2$/2024Al composites (x = 1, 2, 4, 6, 8 wt.%); the misorientation angle distribution of (g) 2024Al, (h-l) xTiB$_2$/2024Al composites, corresponding 001 pole figures are placed in the images, (m) area fraction of HAGBs and LAGBs in as-printed samples.

shows the distribution of the misorientation angle for the as-printed 2024 alloy and xTiB$_2$/2024Al composites. The as-printed 2024Al alloy presents a high fraction of LAGBs (40.4% of the total grain boundary). The mobility of LAGBs is significantly lower than that of the HAGBs [25]. LAGBs are randomly distributed in 2024Al alloy and cannot provide good interaction with dislocations. The as-printed xTiB$_2$/2024Al composites contain a higher fraction of HAGBs associated with sub-grains (Figure 2(m)). This is significantly higher than that obtained in traditional thermomechanical processed Al alloys which present a HAGBs'fraction of 50-65% [26]. The high fraction of HAGBs suggests that xTiB$_2$/2024Al composites have a higher dislocation density and can effectively hinder the dislocation movement during plastic deformation.

The low index 100 stereographic projections in the image inset of Figure 2(g-l), indicated the absence of predominant crystallographic texture in the as-printed xTiB$_2$/2024Al composites. The 2024Al alloy identified the $<100>$ texture along the building direction. Columnar grains prefer to grow along $<100>$ in the build direction as the growth direction has a higher accommodation coefficient compared to other directions in the FCC structure [27]. Texture index equals 1 when a microstructure exhibits isotropy. The stronger the anisotropy, the greater the index deviation from 1. Texture index gradually decreased and stabilized in a range with TiB$_2$ particles addition from $\sim$8.08 for 2024Al alloy to $\sim$2.82 for 8TiB$_2$/2024Al composite.

Figure 2 revealed fine equiaxed grains and a random texture in the as-printed xTiB$_2$/2024 composite, which was attributed to the combined effect of both grain refinement by nano-TiB$_2$ particles and the high cooling rate (10^3-10^6 K/s) [28] of LPBF process. Theoretically, equiaxed grain formation requires two conditions, great undercooling and sufficient heterogeneous nucleation sites [29]. The degree of undercooling is closely related to the cooling rate. The faster the cooling rate, the lower the actual crystallization temperature, and the greater the degree of undercooling. The cooling rate ($\dot{T}$) can be calculated by Rosenthal's equation [30]:

$$T = T_0 + \frac{P_0}{2\pi Rk}\exp\left(\frac{-v(\varepsilon + R)}{2\alpha}\right) \tag{2}$$

where T is the local temperature of the melt pool, R is the distance from the heat source ($R = \sqrt{\varepsilon^2 + y^2 + z^2}$, ε is the distance from the beam position along with TD, y is the distance parallel to the melt surface along with SD, and z is the depth below the melt surface).

Tang et al. [31] showed that the following equation (derived from Equation (2)) can be used to estimate the surface cooling rate of the melt pool:

$$\dot{T} = 2\pi k(T_S - T_0)(T_L - T_0)\frac{v}{P_0} \tag{3}$$

where the plate temperature T_0 is 308 K, the thermal conductivity k is 175 W/mK, the laser scanning speed v is 83 mm/s, the absorption power P_0 ($P_0 = \omega P$, ω is laser absorptivity, taken as 0.19 (Figure 1(f), P is the laser power, taken as 250 W), the thermal diffusivity α is 7.4×10^{-5} m^2/s, and R taken as focused beam spot diameter 75 μm. The solidus temperature T_S (taken as 778 K) and the liquidus temperature T_L (taken as 914 K) were calculated by JMatPro software. Based on Equation (3), $\dot{T}$ can be calculated to be 3.127×10^3 K/s, which is significantly higher than those of the conventional casting method with the cooling medium as Fe and air (0.05 $\sim$ 1 K/s, [32]).

The high cooling rate (3.127×10^3 K/s) provided by LPBF is insufficient to trigger CET. Under the conditions studied, the grain nucleation mechanism is governed by heterogeneous nucleation based on the CET model proposed by Hunt et al. [29]. According to the Edge-to-Edge matching model [33], TiB$_2$ particles are heterogeneous nucleation sites for α-Al because TiB$_2$ particles have many matching interfaces with α-Al and the detailed discussion is shown in *Supplementary material*.

Figure 3(a) shows that the average grain size decreased from 43.51 ± 6.78 μm for 2024Al alloy to 9.05 ± 2.18 μm for 1TiB$_2$/2024Al composite, and continuously decreased with the increase of particle content, while for 8TiB$_2$/2024Al composite reached approximately 3.3 ± 0.46 μm which is one-fifteenth of that of 2024Al alloy. The composite presents a duplex microstructure. As the TiB$_2$ particles content increases, the proportion of columnar crystals gradually decreases, and the content of equiaxed crystals gradually increases, see Figure 3(b). The heterogeneous nucleation of TiB$_2$ particles promotes the generation of equiaxed crystals. Figure 3(c) provides the average equiaxed grain diameters of 6.32 ± 1.32, 5.54 ± 0.58, 4.63 ± 0.35, 3.85 ± 0.47, and 3.54 ± 0.33 μm for the composite with 1wt.%, 2wt.%, 4wt.%, 6wt.%, and 8wt.%TiB$_2$, respectively. The interdependence model reveals that the grain refinement mechanism can be used to quantify the effects of TiB$_2$ particle nucleation potency and particle concentration on grain size [34]. The empirical relationship between equiaxed grain size, d, and particle contents was evaluated by Easton and StJohn [35]:

$$d = \frac{a}{\sqrt[3]{w}} + \frac{b}{Q} \tag{4}$$

where a, b, is the fitting factors for the existing data in a wide range of Al alloys, Q is the growth restriction factor, detailed calculation method is shown in *Supplementary material*.

Equation (4) is used to study the relationship between particles content and grain size. It is found that the solute atoms play a significant role in the variation of Q value. For a certain material system, Q value doesn't vary with particles addition and is equal to 16.59 in this study. There is a quantitative relationship between particles content and grain size, so this formula is used for fitting the experimental result. Figure 3(d) shows that the results of linear regression with experimental grain size, the fitted R^2 value of 0.95 indicates a good fitting between grain size and reciprocal of the cube root of the particle content, see Equation (5):

$$d = \frac{6.62}{\sqrt[3]{w}} + 0.29 \tag{5}$$

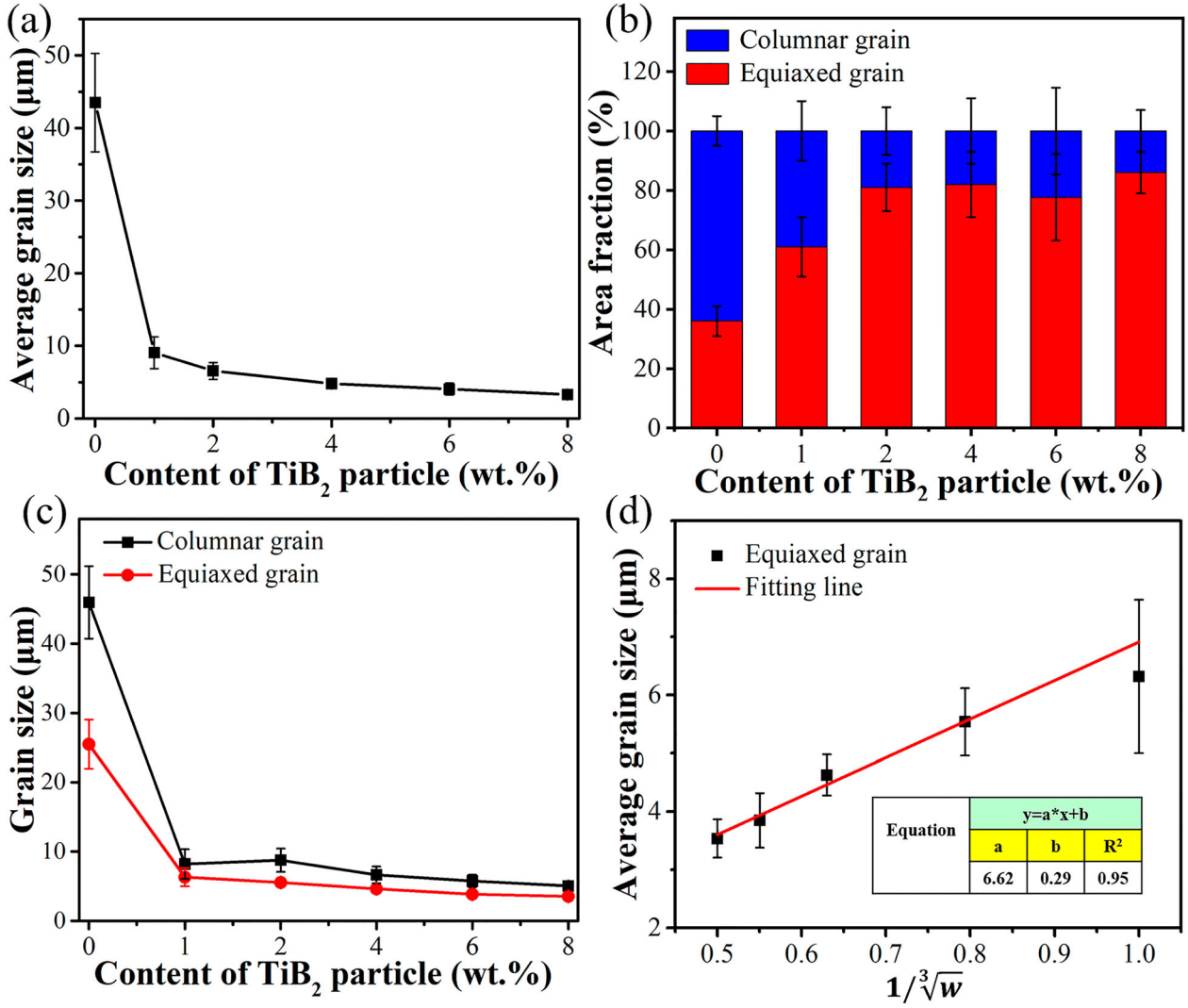

Figure 3. (a) Average grain size of the as-printed samples, (b) area fraction of the columnar and equiaxed grain, (c) distinct columnar and equiaxed grain size, (d) plot of the grain size vs the inverse cube root of the TiB_2 content for the present work.

By analyzing the effects of TiB_2 particle concentration on grain size, Equation (5) can be used to estimate grain size refined by TiB_2 particle for the solidification conditions used in this work. This means that when alloy and the inoculator contents are determined, the grain size can be predicted under fast solidification conditions. This provides a tool for understanding the function of grain refinement and optimizing the content of the TiB_2 particles in Al alloys.

Figure 4(a) shows the average hardness values of the as-printed 2024Al alloy and xTiB$_2$/2024Al composite on the SD-BD plane. The hardness of the 2024Al alloy under the same conditions was ~108 HV, which is ~35% higher than the equivalent 2024-O sheets (60-90 HV [36]). In addition, TiB_2 particle results in a significant increase in hardness. With the addition of TiB_2 particles from 1wt.% to 8 wt.%, the hardness continuously increased. The 8TiB$_2$/2024Al composite showed a high hardness of ~125 HV which is only ~10% less than that of the T6-treated conventionally-processed 2024-T6 sheet (typical 135–145 HV [37]). The increase in hardness can be attributed to the restriction of dislocation motion because of the increase in the dislocation density, the presence of the TiB_2 nanoparticles within the matrix, and the grain refinement effect. Here, multiple strengthening mechanisms affect the hardness and deduce the dominant strengthening mechanism for the as-printed xTiB$_2$/2024Al composite. The results of the present assessment of the grain boundaries hardening by grain refinement, solid solution hardening, and Orowan-strengthening by TiB_2 particles increment are presented in Figure 4(b), detailed calculation method shown in *Supplementary material*.

Figure 4(c, d) shows the tensile tests performed on as-printed samples. 2024Al alloy had a low strength (180 MPa) and ductility (0.3%) along with TD due to the

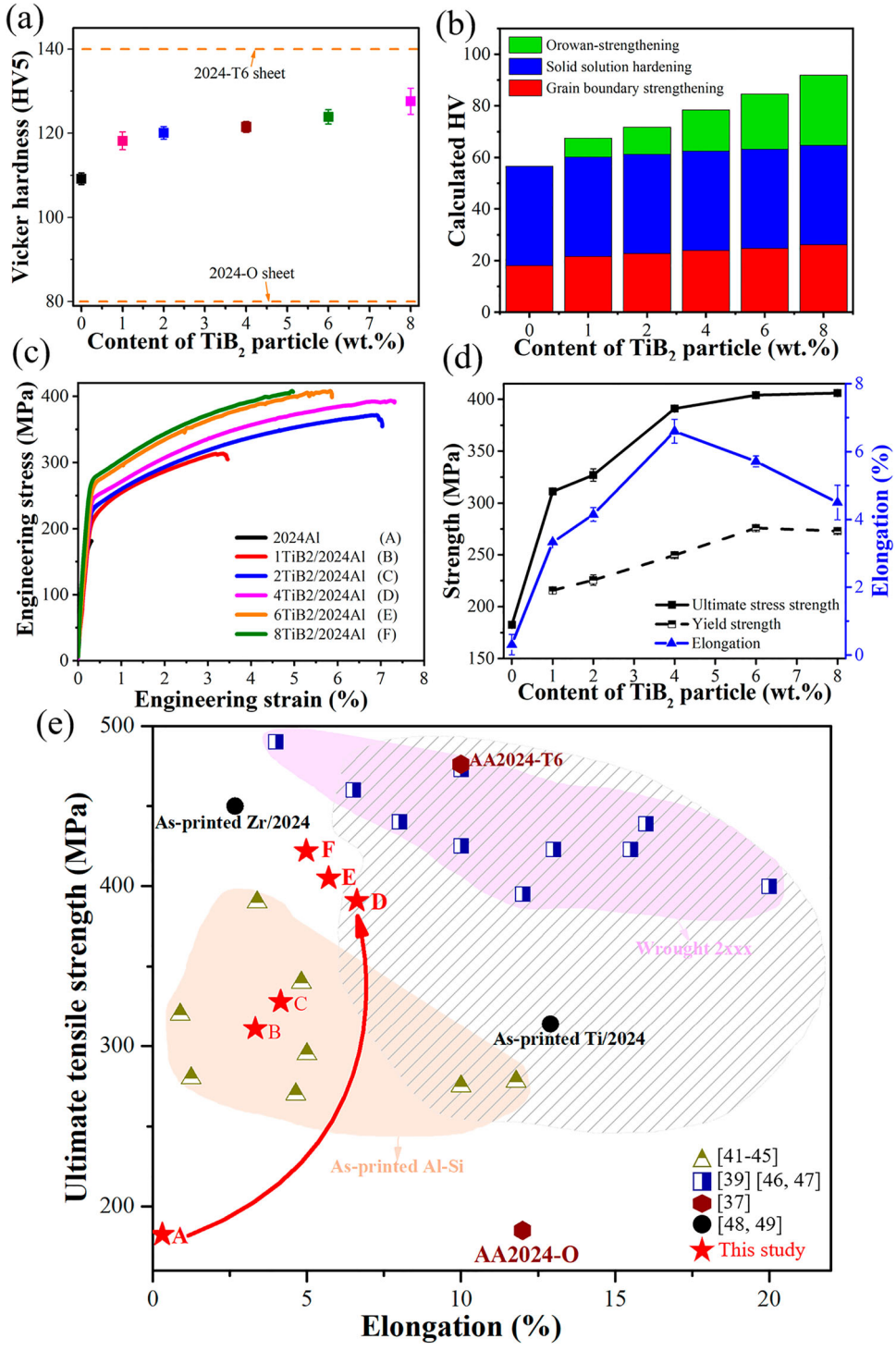

Figure 4. (a) Average Vickers hardness values, (b) multiple strengthening increment of the HV, (c) tensile stress-strain curves, (d) comparison of strength and ductility of the as-printed samples, (e) mechanical properties comparison of the present as-printed samples with reference [37, 39, 41–49].

high density of pores (see Figure 1(a)). The strength and ductility are improved simultaneously when TiB_2 nanoparticles are introduced. With the addition of TiB_2 particles, tensile strength increased continuously and reached its maximum value at $8TiB_2$/2024Al composite, which was 422 ± 3.1 MPa. While the elongation of the samples increased with the particle content at first, and reached its maximum value in the $4TiB_2$/2024Al composite ($6.62 \pm 0.35\%$) and then decreased with the further increase of particle content to $4.98 \pm 0.51\%$ in $8TiB_2$/2024Al composite. Ductility behavior is the result of the competition between deformation plastic by

dislocation generation and motion at stress sources with the fracture by atomic decohesion. When the addition content of particles was less than 4wt.%, TiB_2 particle improved the printability of the 2024Al alloy with the low volume fraction of pores (see Figure 1(b-d)), while the increase of ductility is controlled by dislocation behavior. It is determined that the impact of cracks in the fracture process weakened and the impact of dislocation activities in the fracture process increased with TiB_2 particle addition. When the addition of TiB_2 content was higher than 4wt.%, the large volume fraction of pores formed during LPBF (see Figure 1(e-f)) would influence the fracture process. Furthermore, the high content of TiB_2 particles would change the dislocation activities and induced the reduction of the elongation [38].

Figure 4(e) compares the mechanical properties of the present as-printed 2024Al alloy and alloys with other commercial Al–Si and 2xxx alloys fabricated by LPBF and conventional wrought 2xxx alloys. The as-printed $x$$TiB_2$/2024 composites exhibited excellent performance in both strength and ductility, which was superior to most as-printed Al–Si [41-45] and 2024Al alloys [48, 49], and was comparable to their conventionally wrought manufactured 2024Al alloy counterparts [39, 46, 47]. The quality indices combining both tensile strength and elongation in a single quantity was adopted as the criterion of Al alloy mechanical properties [39]. Generally, Al alloys which are potential to be used as structural materials require the quality indices larger than the value of 2500 [40] (see the shaded area in Figure 4(e)). The quality indices of 4TiB_2/2024Al composite located in the shaded portion indicated that it met this requirement. The 4TiB_2/2024Al composite with a good combination of strength and ductility can be further enhanced through suitable post-heat-treatment. Hence, replacing the wrought 2024Al part with the LPBFed one behaves great potential.

4. Conclusions

We successfully decipher the efficiency of *in-situ* nano-TiB_2 particles in improving the printability of non-castable 2024Al alloy by cut-edge experiment and mathematical model. The as-printed $x$$TiB_2$/2024Al composites show weak texture and duplex-microstructure with refined grains, and the average grain sizes decreased consistently with the increase of TiB_2 content. The quantified relationship between the grain size and the predecorated TiB_2 particles content ($d = \frac{6.6}{\sqrt[3]{w}} + 0.29$) was established, which can be used to predict and control the microstructure manufactured by LPBF. Furthermore, the optimized mechanical properties of the as-printed $x$$TiB_2$/2024Al composites are comparable to its conventionally fabricated wrought 2024Al alloys, proving the feasibility of replacing the wrought part with the LPBFed one.

Credit authorship contribution statement

Tengteng Sun: Investigation, Validation, Writing – original draft. **Hongze Wang**: Conceptualization, Funding acquisition, Formal analysis, Writing – review & editing. **Zhenyang Gao**: Data curation, Formal analysis, Writing – review & editing. **Yi Wu**: Investigation, Resources, Formal analysis, Writing – review & editing. **Mingliang Wang**: Conceptualization, Resources, Formal analysis, Writing – review & editing. **Xinyuan Jin**: Data curation, Formal analysis, Writing – review & editing. **Chu Lun Alex Leung**: Data curation, Formal analysis, Writing – review & editing. **P.D. Lee**: Data curation, Formal analysis, Writing – review & editing. **Yanan Fu**: Resources, Writing – review & editing. **Haowei Wang**: Supervision, Writing – review & editing.

Acknowledgements

This work is sponsored by National Natural Science Foundation of China (52075327 and 52004160), Shanghai Sailing Program (20YF1419200), Natural Science Foundation of Shanghai (20ZR1427500) and Major Science and Technology Project of Huaibei (Z2020001).This project has received funding from the European Union's Horizon 2020 research and innovation programme under the Marie Sklodowska-Curie grant agreement No 896742.

Disclosure statement

No potential conflict of interest was reported by the authors.

Funding

This work was supported by National Natural Science Foundation of China: [Grant Number 52004160, 52075327].

References

[1] Liu Z, Zhao D, Wang P, et al. Additive manufacturing of metals: microstructure evolution and multistage control. J Mater Sci Technol. 2022;100:224–236.
[2] Sing SL, Kuo CN, Shih CT, et al. Perspectives of using machine learning in laser powder bed fusion for metal additive manufacturing. Virtual Phys Prototyp. 2021;16(3):372–386.
[3] Wang D, Liu L, Deng G, et al. Recent progress on additive manufacturing of multi-material structures with laser powder bed fusion. Virtual Phys Prototyp. 2022;17(2):329–365.
[4] Aboulkhair NT, Simonelli M, Parry L, et al. 3D printing of aluminium alloys: additive manufacturing of aluminium alloys using selective laser melting. Prog Mater Sci. 2019;106:100578.

[5] Zhang H, Gu D, Dai D. Laser printing path and its influence on molten pool configuration, microstructure and mechanical properties of laser powder bed fusion processed rare earth element modified Al-Mg alloy. Virtual Phys Prototyp. 2022;17(2):308–328.
[6] Sha G, Marceau RKW, Gao X, et al. Nanostructure of aluminium alloy 2024: segregation, clustering and precipitation processes. Acta Mater. 2011;59(4):1659–1670.
[7] Cheng S, Zhao YH, Zhu YT, et al. Optimizing the strength and ductility of fine structured 2024 Al alloy by nano-precipitation. Acta Mater. 2007;55(17):5822–5832.
[8] Ghaini FM, Sheikhi M, Torkamany MJ, et al. The relation between liquation and solidification cracks in pulsed laser welding of 2024 aluminium alloy. Mater Sci Eng A. 2009;519(1-2):167–171.
[9] Liu X, Liu Y, Zhou Z, et al. Grain refinement and crack inhibition of selective laser melted AA2024 aluminum alloy via inoculation with TiC–TiH_2. Mater Sci Eng A. 2021;813:141171.
[10] Zhou SY, Su Y, Wang H, et al. Selective laser melting additive manufacturing of 7xxx series Al-Zn-Mg-Cu alloy: cracking elimination by co-incorporation of Si and TiB_2. Addit Manuf. 2020;36:101458.
[11] Han C, Babicheva R, Chua JDQ, et al. Microstructure and mechanical properties of (TiB + TiC)/Ti composites fabricated in situ via selective laser melting of Ti and B_4C powders. Addit Manuf. 2020;36:101466.
[12] Martin JH, Yahata BD, Hundley JM, et al. 3D printing of high-strength aluminium alloys. Nature. 2017;549(7672):365–369.
[13] Koh HK, Moo JGS, Sing SL, et al. Use of fumed silica nanostructured additives in selective laser melting and fabrication of steel matrix nanocomposites. Materials (Basel). 2022;15(5):1869–1879.
[14] Zhang X, Xiao Z, Yu W, et al. Influence of erbium addition on the defects of selective laser-melted 7075 aluminium alloy. Virtual Phys Prototyp. 2021;17(2):406–418.
[15] Fan Z, Wang Y, Zhang Y, et al. Grain refining mechanism in the Al/Al–Ti–B system. Acta Mater. 2015;84:292–304.
[16] Li W, Yang Y, Liu J, et al. Enhanced nanohardness and new insights into texture evolution and phase transformation of TiAl/TiB_2 in-situ metal matrix composites prepared via selective laser melting. Acta Mater. 2017;136:90–104.
[17] Thapliyal S, Shukla S, Zhou L, et al. Design of heterogeneous structured Al alloys with wide processing window for laser-powder bed fusion additive manufacturing. Addit Manuf. 2021;42:102002.
[18] Trapp J, Rubenchik AM, Guss G, et al. In situ absorptivity measurements of metallic powders during laser powder-bed fusion additive manufacturing. Appl Mater Today. 2017;9:341–349.
[19] Leung CLA, Marussi S, Towrie M, et al. Laser-matter interactions in additive manufacturing of stainless steel SS316L and 13-93 bioactive glass revealed by in situ X-ray imaging. Addit Manuf. 2018;24:647–657.
[20] Ma C, Zhao J, Cao C, et al. Fundamental study on laser interactions With nanoparticles-reinforced metals—part II: Effect of nanoparticles on surface tension, viscosity, and laser melting. J Manuf Sci Eng. 2016;138(12):121002.
[21] Leung CLA, Elizarova I, Isaacs M, et al. Enhanced near-infrared absorption for laser powder bed fusion using reduced graphene oxide. Appl Mater Today. 2021;23:101009.
[22] Roscoe R. The viscosity of suspensions of rigid spheres. Br J Appl Phys. 2002;3(8):267.
[23] AlMangour B, Grzesiak D, Yang J-M. Nanocrystalline TiC-reinforced H13 steel matrix nanocomposites fabricated by selective laser melting. Mater Des. 2016;96:150–161.
[24] Sun TT, Xiao YK, Luo GD, et al. Roadmap to improve the printability of a non-castable alloy for additive manufacturing. Metall Mater Trans A. 2022;30(4):1–16.
[25] Rollett A. Recrystallization and related annealing phenomena. Australia: Elsevier; 1995.
[26] Eddahbi M, McNelley TR, Ruano OA. The evolution of grain boundary character during superplastic deformation of an Al-6 pct Cu-0.4 pct Zr alloy. Metall Mater Trans A. 2001;32(5):1093–1102.
[27] Jones BL, Weston GM. Orientation relations between dendrites grown in a highly undercooled melt. J Cryst Growth. 1970;7(2):143–146.
[28] Olakanmi EO, Cochrane RF, Dalgarno KW. A review on selective laser sintering/melting (SLS/SLM) of aluminium alloy powders: processing, microstructure, and properties. Prog Mater Sci. 2015;74:401–477.
[29] Hunt JD. Steady state columnar and equiaxed growth of dendrites and eutectic. Mater Sci Eng. 1984;65(1):75–83.
[30] Rosenthal D. Mathematical theory of heat distribution during welding and cutting. Weld. J. 1941;20:220–234.
[31] Tang M, Pistorius PC, Narra S, et al. Rapid solidification: selective laser melting of AlSi10Mg. JOM. 2016;68(3):960–966.
[32] Becker H, Bergh T, Vullum PE, et al. Effect of Mn and cooling rates on α-, β- and δ-Al–Fe–Si intermetallic phase formation in a secondary Al–Si alloy. Materialia. 2019;5:100198.
[33] Ma Y, Addad A, Ji G, et al. Atomic-scale investigation of the interface precipitation in a TiB_2 nanoparticles reinforced Al-Zn-Mg-Cu matrix composite. Acta Mater. 2020;185:287–299.
[34] StJohn DH, Qian M, Easton MA, et al. The interdependence theory: The relationship between grain formation and nucleant selection. Acta Mater. 2011;59(12):4907–4921.
[35] Easton M, StJohn D. An analysis of the relationship between grain size, solute content, and the potency and number density of nucleant particles. Metall Mater Trans A. 2005;36(7):1911–1920.
[36] Wen XL, Wang QZ, Mu Q, et al. Laser solid forming additive manufacturing TiB_2 reinforced 2024Al composite: microstructure and mechanical properties. Mater Sci Eng A. 2019;745:319–325.
[37] Zhang H, Zhu HH, Qi T, et al. Selective laser melting of high strength Al-Cu-Mg alloys: processing, microstructure and mechanical properties. Mater Sci Eng A. 2016;656:47–54.
[38] Xiao YK, Chen H, Bian ZY, et al. Enhancing strength and ductility of AlSi10Mg fabricated by selective laser melting by TiB_2 nanoparticles. J Mater Sci Technol. 2022;109:254–266.
[39] Pantelakis SG, Alexopoulos ND. Assessment of the ability of conventional and advanced wrought aluminum alloys

for mechanical performance in light-weight applications. Mater Des. 2008;29(1):80–91.
[40] Zheng RX, Sun YB, Ameyama K, et al. Optimizing the strength and ductility of spark plasma sintered Al 2024 alloy by conventional thermo-mechanical treatment. Mater Sci Eng A. 2014;590:147–152.
[41] DebRoy T, Wei HL, Zuback JS, et al. Additive manufacturing of metallic components - process, structure and properties. Prog Mater Sci. 2018;92:112–224.
[42] Casati R, Nasab MH, Coduri M, et al. Effects of platform Pre-heating and thermal-treatment strategies on properties of AlSi10Mg alloy processed by selective laser melting. Metals (Basel). 2018;8(11):954.
[43] Read N, Wang W, Essa K, et al. Selective laser melting of AlSi10Mg alloy: process optimisation and mechanical properties development. Mater Des. 2015;65:417–424.
[44] Wang LF, Sun J, Yu XL, et al. Enhancement in mechanical properties of selectively laser-melted AlSi10Mg aluminum alloys by T6-like heat treatment. Mater Sci Eng A. 2018;734:299–310.
[45] Kang N, Coddet P, Dembinski L, et al. Microstructure and strength analysis of eutectic Al-Si alloy in-situ manufactured using selective laser melting from elemental powder mixture. J Alloys Compd. 2017;691:316–322.
[46] Handbook A. Aluminum and aluminum alloys: ASM Specialty Handbook. Materials Park, OH:Asm International. 1993.
[47] Committee AH. Properties and selection: Nonferrous alloys and special-purpose materials. Properties and Selection: Nonferrous Alloys and Special-Purpose Materials. 1990;2:62–122.
[48] Tan QY, Zhang JQ, Sun Q, et al. Inoculation treatment of an additively manufactured 2024 aluminium alloy with titanium nanoparticles. Acta Mater. 2020;196:1–16.
[49] Zhang H, Zhu HH, Nie XJ, et al. Effect of zirconium addition on crack, microstructure and mechanical behavior of selective laser melted Al-Cu-Mg alloy. Scripta Mater. 2017;134:6–10.